PALEONTOLOGY

Cellular remains in a ~3.42-billion-year-old subseafloor hydrothermal environment

Barbara Cavalazzi[1,2]*, Laurence Lemelle[3], Alexandre Simionovici[4,5], Sherry L. Cady[6†], Michael J. Russell[7], Elena Bailo[8], Roberto Canteri[9], Emanuele Enrico[10], Alain Manceau[4], Assimo Maris[11], Murielle Salomé[12], Emilie Thomassot[13], Nordine Bouden[13], Rémi Tucoulou[12], Axel Hofmann[2]

Subsurface habitats on Earth host an extensive extant biosphere and likely provided one of Earth's earliest microbial habitats. Although the site of life's emergence continues to be debated, evidence of early life provides insights into its early evolution and metabolic affinity. Here, we present the discovery of exceptionally well-preserved, ~3.42-billion-year-old putative filamentous microfossils that inhabited a paleo-subseafloor hydrothermal vein system of the Barberton greenstone belt in South Africa. The filaments colonized the walls of conduits created by low-temperature hydrothermal fluid. Combined with their morphological and chemical characteristics as investigated over a range of scales, they can be considered the oldest methanogens and/or methanotrophs that thrived in an ultramafic volcanic substrate.

INTRODUCTION

While Earth may have been a habitable planet long before the Paleoarchean Era [3.6 to 3.2 billion years ago (Ga)] (*1*), as rocks of this age retain a diversity of fossil evidence for life (*2*, *3*), the complexity of life's cellular constituents, range of metabolic pathways, the niches it occupied locally, and global diversity of its habitats remain largely unknown. The Onverwacht Group of the Barberton greenstone belt (BGB) of southern Africa hosts a diverse record of microbial life. Spherical, coccoidal, spindle-shaped, and filamentous microfossils and silicified microbial mats have been reported from marine sedimentary chert units intercalated with a felsic-to-ultramafic volcanic pile (*4*–*7*). Different depositional environments have been proposed, ranging from tidal-influenced shallow marine to deeper water settings on subsiding volcanic platforms (*5*). A close link between chert deposition and synsedimentary, low-temperature hydrothermal activity has been proposed for many of the BGB chert units because of the presence of hydrothermal alteration zones (*8*), cross-cutting chert veins (*9*), and coupled Si-O isotope systematics (*10*). Subseafloor hydrothermal systems generate fluids highly enriched in reduced inorganic chemical species that mix with more oxidized seawater to produce thermal, redox, and proton gradients in a diversity of (micro)habitats (*11*, *12*). In addition to being important for life's early evolution, seafloor hydrothermal systems could have been the first environment to which life adapted or where it first emerged (*11*–*17*). Here, we report the discovery of well-preserved putative filamentous microfossils from a ~3.42-Ga subseafloor hydrothermal vein system from the BGB that provides the oldest evidence for indigenous subsurface microorganisms (section S1) with a methane-based metabolism.

RESULTS

The hydrothermal chert vein system

The hydrothermal chert vein system studied here underlies a marine chert (K1c1) located near the base of the Kromberg Formation of the Onverwacht Group (section S2). The chert unit itself is in stratigraphic continuity with the ~3.42-Ga Buck Reef Chert (*18*) that hosts some of the best-preserved microfossils of the BGB (*4*–*6*). The hydrothermal vein system cuts ultramafic lapillistone that accumulated on a shallow-marine volcanic platform (*19*).

The chert veins are especially common in the uppermost 10 m of the lapillistone, which has been pervasively replaced by carbonate and silica (section S2). Filled by several generations of carbonaceous matter (CM) and chert precipitate (I, II, and III in Fig. 1A; section S3), the veins are generally oriented subparallel to the paleoseafloor, sometimes branching, and range from a few millimeters to several centimeters in width. Similar to chert veins elsewhere in the Onverwacht Group (*9*, *20*), the abundance of angular host rock fragments with a jigsaw fit (section S3) indicates that the veins originated due to hydraulic fracturing. The vein-filling CM consists largely of sand-sized grains, a common microfacies of Archean bedded cherts (*4*, *5*), suggesting derivation from overlying unconsolidated seafloor sediments.

Filaments at the vein–host rock interface

Filaments were found exclusively in two thin (tens to hundreds of micrometers thick) layers (I_a and I_b) of the first generation of chert vein infill (sections S2 and S3). The geometry of I_a (section S3) differs depending on whether it coats the footwall or hanging wall (Fig. 1). Along the footwall, the host rock–chert layer I_a interface is planar and abrupt. Here, I_a consists of a concordant sequential series of planar to botryoidal microlaminae of chert with finely disseminated CM (Fig. 1, B and C, and fig. S3). Chert layer I_b (~200 μm

[1]Dipartimento di Scienze Biologiche, Geologiche e Ambientali, Università di Bologna, Bologna, Italy. [2]Department of Geology, University of Johannesburg, Johannesburg, South Africa. [3]LGL-TPE, ENS de Lyon, Université de Lyon, CNRS, Lyon, France. [4]ISTerre, University of Grenoble-Alpes, CNRS, Grenoble, France. [5]Institut Universitaire de France, Paris, France. [6]Pacific Northwest National Laboratory, EMSL, Richland, WA, USA. [7]Dipartimento di Chimica, Università degli Studi di Torino, Torino, Italy. [8]WITec GmbH, Ulm, Germany. [9]FBK—Fondazione Bruno Kessler, Trento, Italy. [10]INRiM, Istituto Nazionale di Ricerca Metrologica, Torino, Italy. [11]Dipartimento di Chimica "Giacomo Ciamician," Università di Bologna, Bologna, Italy. [12]European Synchrotron Radiation Facility, Grenoble, France. [13]Université de Lorraine, CNRS, CRPG, Nancy, France.
*Corresponding author. Email: barbara.cavalazzi@unibo.it
†Present address: Department of Geology and Center for Life in Extreme Environments, Portland State University, Portland, OR 97201, USA.

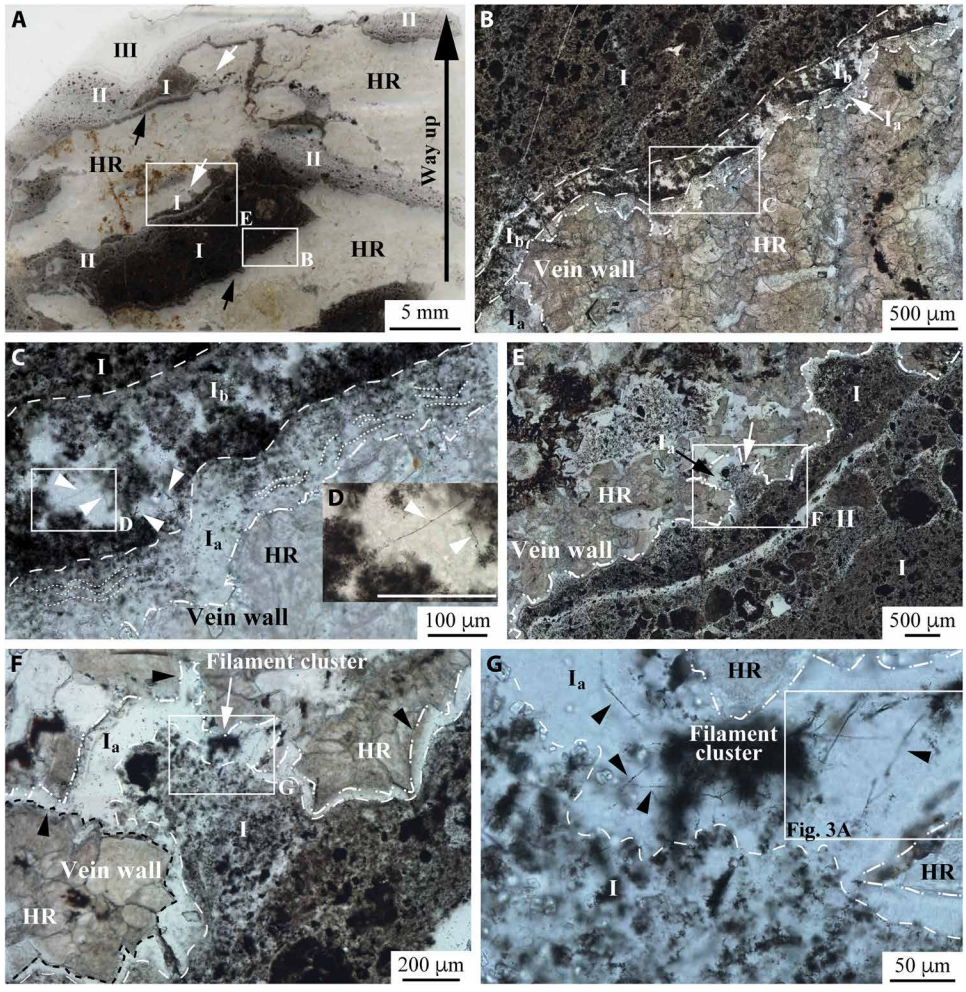

Fig. 1. Paleoarchean filaments in hydrothermal chert veins. (**A**) Scan of a thin section in stratigraphic orientation. The image shows the carbonate-replaced lapillistone host rock (HR) cut by several veins filled with carbonaceous chert (I and II) with different CM:chert cement ratios and cavity-fill (botryoidal) chert (III) (figs. S6 and S7). The labeled boxed areas in each transmitted light photomicrograph are magnified in the following photo. Photomicrographs in (**B**) to (**D**) illustrate details of the vein footwall, whereas (**E**) to (**G**) show the vein hanging wall. Isolated and intertwined filaments [arrows in (C) and (D)] occur in a regularly spaced framework that occasionally span the width of chert layer I_b of the footwall, whereas only isolated clusters of filaments were identified in chert layer I_a [arrows in (E) and (F)] of the hanging wall, typically within cusp-shaped cavities [white arrows in (A)]. (G) High concentrations of individual filaments (arrows) in the bundles of filaments extend outward from filament clusters located in chert layer I_a of the hanging wall. Scale bar in (D), 100 µm.

thick) overlies I_a of the footwall and displays a regularly spaced and vertically oriented framework of CM embedded in chert (Fig. 1, B and C, and fig. S8, C and E) reminiscent of a silicified biofilm. The framework of the biofilm contains filaments that extend upward and outward away from the framework into open space that was ultimately filled by chert precipitate (Fig. 1, C and D, and fig. S8, C to G). The surface of the hanging wall, in contrast to the topology of the footwall, is highly irregular and contains cusp-shaped cavities pointing toward the host rock (Fig. 1, E and F), suggestive of host rock dissolution. The hanging wall host rock is coated by a variably thick chert layer I_a, which lacks lamination and intergrown CM. Filaments occur in I_a as tangled three-dimensional (3D) clusters and are restricted to the cusp-shaped cavities (Fig. 1, A and E to G, and fig. S8, A and B).

Individual linear, narrow unbranched filaments ≤110 µm long (average length: 42 ± 17 µm on 81 filaments; section S4) are (in thin section) brown-black in optical transmitted light with diameters of ~0.5 to ~1.1 µm (average diameter: 0.77 ± 0.07 µm on 81 filaments; section S4) (Figs. 1G, 2A, and 3A and fig. S8). Locally merging and/or overlapping filaments impair direct measurement of the filament diameters along their full lengths. They are commonly disarticulated into 10- to 20-µm segments (Fig. 3A and fig. S8, E and F).

Chemical composition of the filaments

A combination of in situ analyses was used to correlate the chemistry and morphology in a search for biochemical signatures. Time-of-flight secondary ion mass spectrometry (ToF-SIMS) ion maps were used to record the location of filaments that intersected the sample surface (Fig. 2A), which enabled precise correlation of the filaments with H^-, C^-, C_2^-, CN^-, and C_3^- molecular fragments (Fig. 2). Distinct types of CM in the quartz matrix were identified by slight spectral differences in their Raman D-G bands in the range of ~1350

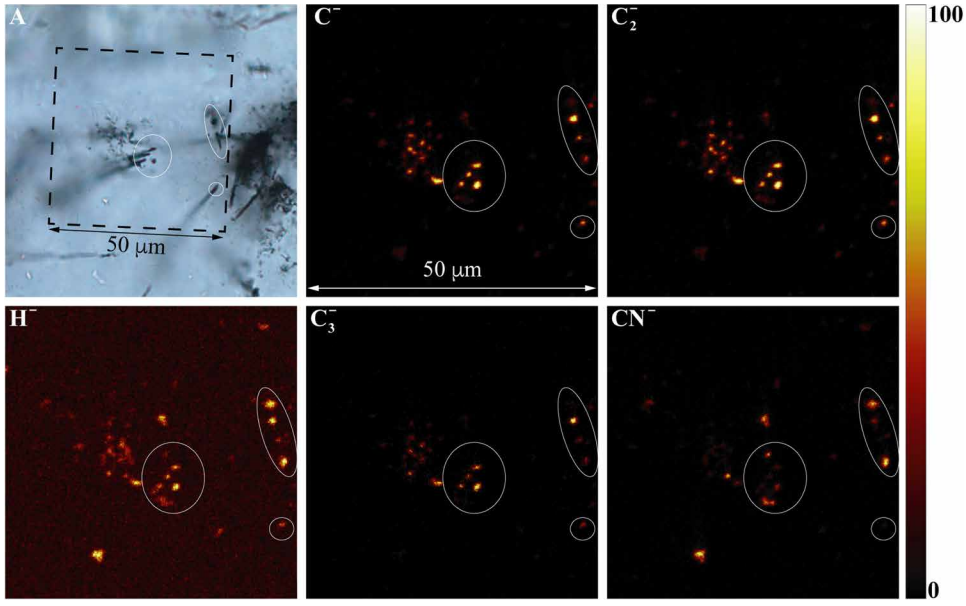

Fig. 2. Representative ToF-SIMS 2D (XY) maps (negative ions) of Paleoarchean filaments. ToF-SIMS images correspond to the boxed area shown in the transmitted light optical photomicrograph (**A**), which captures the topmost surficial focal plane of the petrographic thin section. The ellipses shown in all images are from the same areas on the thin section where filaments clearly intersect the surface. Concentrations of carbon (C^-, C_2^-, and C_3^-), nitrile (CN^-), and hydrogen (H^-) on the mapped surface were visibly colocated with the filaments. In the ToF-SIMS maps, brighter color indicates higher relative signal intensity of the assigned element (see also intensity column).

and ~1600 cm^{-1}, typical for low–structural order CM (Fig. 3, B and C, and fig. S11). 3D confocal Raman imaging highlights the spatial distribution of the filaments and the variable chemical nature of its CM (Fig. 3). Most notable is the nested distribution of two spectrally distinct CM types in association with the filaments (D-G: 1337 and 1573 cm^{-1} and 1346 and 1590 cm^{-1}, respectively): one comprising the inner filament and the other occurring as a laterally discontinuous external coating (Fig. 3B and movie S1). A third type of CM is associated with nanoparticles (~0.35 μm in diameter; D and G: 1350 and 1589 cm^{-1}) dispersed throughout the quartz matrix (Fig. 3B).

Individual filaments in the α-quartz matrix were investigated by high-angle annular dark-field scanning transmission electron microscopy (HAADF-STEM) and electron energy-loss spectroscopy (EELS) (Fig. 4). STEM imaging reveals the irregular shape of their cross sections with diameter ranging between ~450 and 800 nm (Fig. 4A). A moderately ordered nature of the CM (organic material or kerogen) detected in the filament core (Fig. 4, C and D) is indicated by the small π* shoulder (~285 eV) followed by a wide region σ* peak (~297 eV) with a shallow slope on the high-energy side, which lacks the sharp peak of the C K-edge typical of graphite [Fig. 4D; EELS reference spectra (*21*)].

Synchrotron nano–x-ray fluorescence (XRF) imaging carried out on focused ion beam (FIB) sections reveals trace amounts of S and Ni (Fig. 5A and section S6). Synchrotron x-ray micro-XANES (x-ray absorption near-edge spectroscopy) of S exhibits a K-edge energy of 2473.5 eV, corresponding to that of a heterocyclic sulfide (section S6). Nickel K-edge spectra, acquired by nano-XANES (section S6), were used to constrain the possible molecular groups linked to Ni. The spectrum of the filament in Fig. 5B displays a K-edge value (8343.2 ± 0.25 eV) 2.4 eV higher than that of a NiO standard, ruling out Ni-bearing silicate minerals in the filament, as well as Ni(0) metal and Ni(I/II) sulfides and inferring organo-Ni complexes of mixed Ni(II) and Ni(III) valencies (*22*).

DISCUSSION

To understand the origin and nature of the studied filaments, morphological and chemical signatures require evaluation regarding biogenicity (section S4). The reconstructed ecological setting provides further constraints on interpreted metabolic pathways.

Filamentous microfossils

Although a plausible biological morphology alone is not decisive proof of the microbial origin of the filamentous structure, it is a required criterion for identifying microbial fossils (section S4) (*3*, *23*–*25*). Several morphological features of the studied filaments are notably similar to other permineralized microfossil examples found throughout the geological record [e.g., (*4*, *24*–*26*)]. Disarticulation (Fig. 3A and fig. S8, E and F) is a common attribute of fossilized microbial filaments [e.g., (*4*, *24*–*26*)] and could reflect either or both structural (i.e., cell division points) (*23*, *26*) and taphonomic discontinuities (i.e., due to compressions or less preserved and degraded remains) (*2*, *23*, *27*). High morphological 3D fidelity of the filament preservation is consistent with very early and rapid silicification [e.g., (*24*, *28*, *29*)], which is to be expected of Paleoarchean silica-saturated hydrothermal systems (*10*, *19*).

All of the filaments we analyzed here are embedded in (α-quartz) chert (Figs. 3, B and C, and 4, B and C) and are composed of moderately ordered carbon (Fig. 4D), consistent with ancient permineralized kerogenous cellular remains (*23*–*25*). In addition to having a kerogenous composition [also supported by the presence of H, N, and C-N heteroatoms; Fig. 2; e.g., (*30*)], we revealed the nested distribution of (spectrally) different types of molecular carbonaceous compounds associated with some of the filaments. Although the diffusion of the cellular material along quartz crystal boundaries is a known taphonomic or diagenetic effect that could generate around the fossils themselves specific secondary textural patterns including carbonaceous halos, piliform or saw-tooth structures, and semihollow

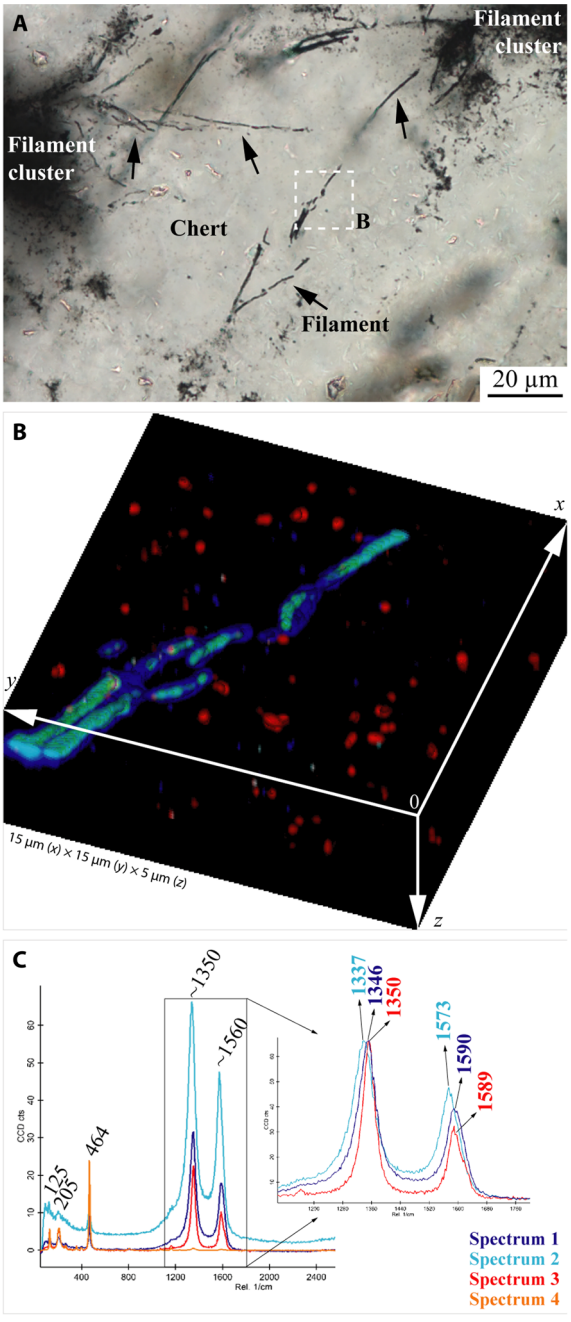

Fig. 3. Distribution of different CM types in the Paleoarchean filaments. (**A**) Extended depth of field transmitted optical photomicrograph (boxed area in Fig. 1G) showing filament details. (**B**) 3D confocal Raman image of the different types of CM detected in association with filaments and surrounding area, corresponding to the boxed area in (A). Color coding here reflects only the different CMs distinguished by different Raman spectra in (C). Turquoise and blue indicate Raman spectra 1 and 2 in (C), respectively, which is associated with the CM of the filaments, whereas red indicates a Raman spectrum 3 in (C) for CM of the nanometric particles dispersed in the chert vein layer I_a. Brighter color corresponds to the greater peak intensity (cf. movie S1). (**C**) Average Raman spectra of each species analyzed in the rendered volume in (B). Magnification of the D and G band region (inset) shows spectral details where the intensity was normalized to that of the D peak (see section S5). All spectra are represented on the same intensity scale. Spectrum 4 corresponds to the matrix quartz composition. Note that the Raman signal of the chert matrix, corresponding to the Raman spectrum 4 in (C), has been removed and appears black in (B).

mold [e.g., (*27*, *31*)], evidences of such processes—i.e., quartz particles wrapped in the kerogen of the filament outer walls and/or carbon redistributed throughout the quartz matrix in the vicinity of the filament periphery—were not observed by high–lateral resolution, high–spatial resolution, and high–spectral resolution investigations (Fig. 3B, movie S1, and fig. S11.1). Furthermore, filaments were not generated by carbonaceous compounds coating crystal surface or intragranularly displaced during recrystallization [e.g., (*31*)]. The carbonaceous external layer could plausibly represent remnants of a cell wall, a cell membrane, an extracellular sheath or envelope, or an extracellular polymeric substance (EPS) component, whereas the core of the "sheathed" filaments could be condensed intracellular or cytoplasmatic matter. In such a case, the nested correlation of cell and outer/extracellular features comprised of different forms of CM would reflect an ultrastructural (spectral) elaboration consistent with a cellular origin (*23*), and the local discontinuity of the extracellular features could likely reflect early microbial degradation immediately before early fossilization. The presence of a thin localized, although partially discontinuous, external C layer that is structurally distinct from the kerogenous filament cores and the CM disseminated in the silica matrix (Fig. 3, B and C, and section S5) could reflect differences in the composition of the organic precursors and could be consistent with preservation of the remains of sheath-like or cell wall–like structures (*32*). The nanoscale carbonaceous particles dispersed in the chert matrix (Fig. 3B and section S5) display distinct Raman spectra and likely represent carbonaceous components frequently observed in chert cement (*7*, *33*, *34*). Kerogenous composition of the filaments and carbonaceous nanoscale particles is consistent with low-grade metamorphic overprinting of the central BGB (section S5) (*5*).

The chemical composition of the filaments is consistent with a kerogenous nature and includes most of the major bioessential elements (C, H, O, and N in Fig. 2 and S in fig. S13). The absence of P could be the result of scavenging or leaching of this bioessential element. Moreover, postdepositional taphonomic reworking of heteroatoms would concentrate decay-resistant biopolymers that covalently bond S, N, and C [e.g., (*35*)]. The homogeneous distribution of trace amounts of S (fig. S13) associated with the kerogen in the filaments, along with the sulfide XANES K-edge at 2473.5 eV, suggests the presence of an organic heterocyclic sulfide as previously detected in other Precambrian microfossils (*35*). Organic linear and heterocyclic sulfides are purportedly formed by the aromatization of organics during thermal metamorphism, which stabilizes kerogen (*36*).

The presence of Ni-organic compounds in the filaments (Fig. 5) is consistent with primordial metabolisms (*37*) and not unexpected, given the high bioavailability of Ni on the reducing early Earth and in situ Ni trace detection in ~3.33-Ga-old organic matter (*38*). The cellular levels of Ni enzymes intrinsic to the methanogenic and methanotrophic metabolic pathways of modern microbes (*39*–*41*) are particularly high, as are their Ni contents (*42*–*45*). Ni enzymes, commonly used in anaerobic metabolisms, have also been highly conserved from molecular evolution over geological time (*37*, *46*). Furthermore, the evidence for possible Ni-organic complexes with mixed II/III Ni valencies (*47*) is consistent with cofactors of inactivated enzymes involved in methane-metabolizing pathways. The measured Ni concentrations in the filaments ($2.78 \times 10^7 \pm 1.95 \times 10^6$ at μm^{-3} equivalent to 0.46 ± 0.03 mM) (Fig. 5A) similar to the Ni contents reported for modern methanogenic microbes [e.g., 0.44 ± 0.04 mM in (*45*); see also (*42*–*44*, *48*)] are also consistent with the presence of methanogens and methanotrophs. In addition, several examples of

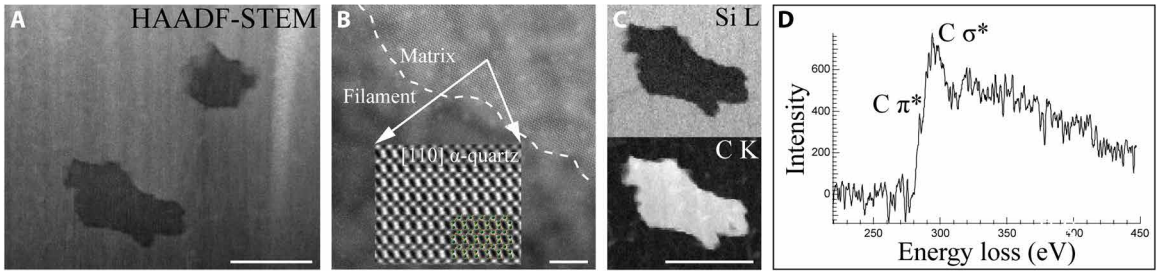

Fig. 4. Ultrastructural organization and chemical composition of the filaments. (**A**) Diameter of sectioned filaments (fig. S10) varies from ~450 nm for equant shape to ~800 nm for non-equant filaments, depending on their orientation relative to the plane of the TEM FIB section. (**B**) Representative HR-STEM image ([110] zone axis; α-quartz) of the contact between the chert matrix and the CM of the large filament in (A). (**C**) EELS maps of silicon (Si) and carbon (C) of a sectioned filament shown in (A). Note the homogeneous distribution of C of the filament and Si dominated the host matrix. (**D**) EELS spectrum from the sectioned filament shown in (C) indicates that the structure is comprised of moderately ordered carbon, kerogen (poorly resolved π* peak and rounded σ* peak). Scale bars, (A) and (C) 500 nm; scale bar, (B), 5 nm.

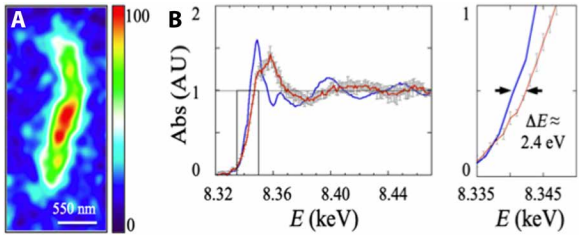

Fig. 5. Nickel in kerogenous filaments. (**A**) High–spatial resolution map of the distribution of Ni (plotted from the Ni Kα line intensity contours that are color-coded on a temperature scale) of a filament analyzed in a (3.1 ± 0.2 μm thick) FIB cross-sectioned filament (fig. S10), recorded at 17 keV on ID16B ESRF (dwell time, 0.5 s; pixel size, 55 nm). The Ni distribution corresponds to the 2D projection of all Ni atoms associated with the filament (throughout the entire FIB section volume; section S6). (**B**) Nano-XANES spectra of the filament (red line) from (A) and of a Rhône-Poulenc NiO standard (blue line). Magnified view (right) of the boxed area (shown in left) details the Δ*E* edge shift used for valence estimation (arrows). Error bars are within the linewidth for NiO and are plotted in gray for the filament. AU, arbitrary units.

methane-cycling microorganisms with slender (>1-μm) straight or curved filaments with walls, septa, or extracellular envelopes (e.g., *Thermofilum*, *Methanosaeta*, and *Crenothrix*) are known.

The filaments satisfy the commonly accepted biogenicity, indigenicity, and syngenicity criteria (section S4). The studied filaments also differ from known abiotic pseudofossils (section S4) in the specific combination of their site of occurrence, 3D morphological complexity, kerogenous nature, spectrally observed ultrastructures, and their specific metal-organic signature. Although biomorphs, produced in the absence of any direct biological activity under geochemical conditions that could have existed on early Earth [e.g., (*49*, *50*)], must be considered when evaluating the biogenicity of putative early trace of life, their features with the various attributes of the filaments described here are currently not known (section S4). Possibly the strongest evidence for the biogenicity of the studied filaments is their occurrence in specific associations (single or in clusters) within different parts of the vein microhabitat and in association with biofilms.

Although cellular fossils of archaeal methanogens and methanotrophs have not yet been reported in the Paleoarchean record (*2*, *3*) and Paleoarchean geochemical evidence (carbon isotopes) for microbially produced methane is limited (*51*), methane-utilizing metabolic pathways are commonly recognized as ancient in origin [e.g., (*3*, *46*)]. Despite the demonstrated fossilization potential of Archaea [e.g., (*29*)], their fossil record is restricted to the Phanerozoic (*2*, *3*, *52*). Our findings could possibly extend this record back to 3.42 Ga.

Archean ecological habitat within a subseafloor hydrothermal system

The fossil assemblage we described here flourished in a paleo-subseafloor setting at the interface of a carbonated ultramafic lapillistone and silica-oversaturated hydrothermal fluid (schematic model in section S3). The hydrothermal processes, likely related to cooling of the underlying volcanic and volcaniclastic rocks following eruption and deposition on the seafloor, generated widespread low-temperature [≤150°C; (*8*, *10*)] diffuse flow systems of seawater chemically modified during water-rock interaction. At ~3.4 Ga, seawater was anoxic (*53*), less alkaline [~neutral pH; (*54*)], and possibly warmer than today [<40°C; (*55*)]. Its interaction with fresh ultramafic rock at depth would have made it more alkaline (*8*) and enriched in biophilic metals such as Ni (*10*). The high pH of subsurface fluids is indicated by pervasive carbonatization of ultramafic rocks at depth, with secondary carbonate having a carbon isotopic composition that indicates that $C_{carbonate}$ was derived from seawater (section S3). A few meters below the paleoseafloor (section S2), large-scale mixing of subsurface fluids with colder and less alkaline seawater following hydraulic fracturing would likely have resulted in the replacement of earlier-formed carbonate by secondary silica, which itself presumably precipitated upon a drop in pH, during ongoing fracturing events that subsequently established new links with the seafloor. Zones with strong geochemical gradients that enhanced water-rock interactions are typically regarded as suitable ecological niches for communities of lithoautotrophs in both past and present subseafloor settings (*14*, *37*).

The irregularity of the upper vein margins suggests dissolution and silica replacement of the host rock, whereas the lower vein margins could have been protected from dissolution by the presence of an actively metabolizing microbial biofilm community that colonized the accretionary surface of the vein wall (I_b). That filament clusters were only found near the end of cusp-shaped cavities of the hanging walls of the vein and that single filaments were associated with what appear to be mottled CM relicts of biofilm on the vein floor clearly indicate variations in the ambient physicochemical conditions and thus multiple potential microbial microhabitats within the veins. This is mirrored by modern vent microbial communities, which are

distributed, due to selective physicochemical forces, within distinct macro- and microenvironmental vein settings (*12*). These environments—typified by moderate hydrothermal temperature, abundant availability of essential nutrients, and steep redox and pH gradients—would have provided the necessary ingredients and free energy to sustain biofilms comprised of acetogens, methanogens, methanotrophs, and heterotrophs (*14*, *37*, *56*). The presence of specific Ni-organic compounds associated with the filaments is consistent with methane-cycling metabolic pathways known to dominate subsurface microbial communities in ultramafic environments (*57*). The CM of subsequent vein-fill generations lacking cellular remains likely originated from planktonic and benthonic material entrained in the downward flow of sediment-laden seawater (section S3) (*8*, *20*, *34*). CM is also found in the lapillistone and dispersed within the chert cement (section S2) and may have formed abiotically, as hydrocarbons derived from subsurface serpentinization reactions and thermal alteration of carbonaceous seafloor sediments [e.g., (*58*, *59*)]. Hydrocarbons would have become entrained in such hydrothermal systems and could have provided further support of methane-cycling microbial assemblages.

In this work, a suite of converging and mutually supportive evidence indicative of biogenicity (morphology and chemical composition) and a favorable ecological setting along with meeting endogenicity and syngenicity criteria (*3*) was established for filaments in a habitable Archean subsurface ultramafic environment. This discovery of microfossils extends knowledge of the early subsurface fossil record and provides a strong case for the importance of subsurface hydrothermal systems as an abode for early life (*11*, *14*). These findings provide the oldest direct evidence for subsurface methane-cycling microorganisms, most likely methanogens, consistent with their expected antiquity based on carbon isotope analysis of fluid inclusions (*51*) and molecular evidence (*46*).

MATERIALS AND METHODS

Optical microscopy

Petrographic analysis, mineralogical identification, and textural observations of the carbonaceous vein cherts were conducted on 30- and 50-μm-thick, uncovered polished thin sections at the Environmental Molecular Sciences Laboratory (EMSL) User Facility at Pacific Northwest National Laboratory (PNNL), Richland, WA, USA, using a transmitted and reflected light Zeiss Axio Imager 2 optical microscope (Carl Zeiss Inc., Germany) equipped with a Nikon DS-5M-L1 digital microscope camera (Nikon Instruments) operated by the Zeiss ZEN 2012 Microscope and Imaging Software from Carl Zeiss Inc. (Germany). The extended depth of field imaging of the Zeiss Extended Focus module applied to some images allowed us to process z-stack images, which resulted in a single image where every object in the image was present at its optimal focus state within the input z-stack.

Time-of-flight secondary ion mass spectrometry

The ToF-SIMS data acquisition was carried out at the EMSL-PNNL in USA on a ToF-SIMS IV instrument (ION-TOF GmbH, Germany). For surface ion mapping on thin sections, the primary ion beam used for analysis was 25 keV of Bi_3^+ as primary ions for analysis, while for soft etching of the uppermost surface, a beam of 10-keV C_{60}^+ ions was used. The etched area was 600 μm by 600 μm, and the analyzed area was 50 μm by 50 μm centered in the etched area. To compensate the sample charging effects, an electron flood gun was used. For surface ion mapping, the primary ion beam was rastered over the analyzed area with a spatial resolution of about 500 nm.

Raman microspectroscopy imaging

Raman spectra were recorded using a WITec Confocal Raman Microscope System alpha300R with an ultrahigh-throughput spectrometer (WITec Inc., Germany) at the Assore Raman Laboratory, University of Johannesburg. Raman signal was collected by using a 100× (numerical aperture of 0.90) Nikon objective (Nikon, Tokyo, Japan) with a Ø 50-μm optic fiber, dispersed by a diffraction grating of 600 grooves/mm, and collected on a Peltier-cooled EMCCD detector. The scans were performed using a frequency-doubled Nd-YAG laser (Newport, Evry, France) providing excitation at a wavelength of 532 nm perpendicular to the sample surface. To prevent laser-induced thermal effects of the samples, the laser excitation intensity was set to the 1.5-mW range at the sample surface, and an adequate signal-to-noise ratio was achieved for a single spectrum per pixel with an acquisition time of 36 ms. Fifteen confocal 2D (*x*-*y*) Raman maps (15 μm by 15 μm, 150 points per line, and 150 lines per image) from different focal planes (5 μm) were acquired at high spectral and spatial resolution (~350 nm in *x* and *y* and ~1.4 μm in *z*) by automatically scanning the sample along the *z* axis (starting at the focal plane oriented parallel to and above the sample surface and extended into the sample at 5-μm step sizes). Data acquisition, evaluation, and processing were performed using the WITec Project Management and Image Project Plus software suite. The data from the image stack were combined to generate the 3D image by using ImageJ and ImageVis3D (*60*).

Dual-beam focused ion beam scanning electron microscopes

The dual-beam FIB scanning electron microscopy (DB FIB-SEM) technique was used to detect, dissect, and prepare ultrathin sections of the filaments (fig. S10) (*61*). FIB sections for TEM (*x*-*y*-*z*: ~5 μm by 5 μm by 0.1 μm) and for nano-XRF and nano-XANES (*x*-*y*-*z*: ~5 μm by 10 μm by 3 μm) investigations were prepared with the use of a DB FIB-SEM FEI Helios at the EMSL-PNNL (Richland, WA, USA) and with a DB FIB-SEM FEI Quanta 3D at INRiM (Torino, Italy). Delicate features below the thin-section surface were targeted to eliminate the risk of surface contamination and were identified by correlating 2D surficial topography and 3D reconstruction information (optical microscopy, ToF-SIMS, and Raman spectroscopy). The ultrathin sections were prepared using low ion currents and energies (at shallow-angle steps in the final ion polishing) to prevent damage to the surface layer and were imaged in SEM imaging mode.

Electron microscopy (HAADF-STEM and EELS)

Two ultrathin cross-sectional electron-transparent specimens (50 to 100 nm thin) were prepared for microstructural and chemical investigations of cell-like morphologies (fig. S10) [the obtained FIB specimens were too thick for high-quality high-resolution TEM (HR-TEM) and EELS data acquisition but were the best compromise to obtain accurate electron-transparent sections, thus avoiding bending or other morphological artifacts]. TEM observations were acquired with the use of a FEI Tecnai G2T-20 and a FEI Titan 80-300 STEM at the EMSL-PNNL, Richland, WA, USA. Atomic imaging modes in STEM enabled the acquisition of HR-TEM phase-contrast images and incoherent annular dark-field STEM (HAADF-STEM) images. Energy-dispersive x-ray spectroscopy and EELS in ADF-STEM

mode provided localized compositional and electronic information. EELS spectra were acquired in STEM mode using a Quantum model Gatan Image Filter with a spectrometer and produced a 3D dataset (x, y, and energy). EELS maps were recorded at 300 keV.

Synchrotron XRF and XANES

Micro– and nano–x-ray imaging were performed at ESRF's ID21 and ID16B beamlines, respectively (section S6), which probe the elemental composition and speciation in the tender (2 to 9 keV) and hard (6 to 30 keV) x-ray energy regions. These undulator beamlines use fixed-exit double-mirror systems for harmonic rejection and fixed-exit double-crystal monochromators (Si_{111}, Kohzu Precision Co. Ltd., Japan) delivering monochromatic beams of energy resolution $\Delta E/E = \sim 2 \times 10^{-4}$. Focusing uses multilayer Kirkpatrick-Baez mirror systems that deliver beam sizes of 750 nm by 300 nm [5×10^9 photons per second (ph/s) at 2.5 keV] and 50 nm by 60 nm (5×10^{11} ph/s at 17 keV) for ID21 and ID16B, respectively. Fluorescence is detected by single-element (ID21) or multielement (ID16B) fast (≤1 mega counts per second) Silicon Drift Diode detectors (Bruker XFlash 5100, 80-mm^2 area and SGX RaySpec, 3 mm by 80 mm). Spectra are collected in "zap" continuous scanning mode, by raster-scanning the sample in front of the focused beam while detectors continuously collect spectra. Maps provide raw counts of element lines per pixel, summed for regions of filaments or matrix to produce high-statistics spectra for semiquantitative analysis parameterization that are necessary to detect trace contrasts [section S6; (*49*)]. S and Ni K-edge XANES spectra were acquired in fluorescence mode in the energy range of 2.46 to 2.5 keV at 0.25 eV per step and 8.27 to 8.47 keV at 1 eV per step, respectively. We used several sulfur standards (Sigma-Aldrich Inc.), a NiO powder standard (Rhône Poulenc S.A., Ø ≤ 5 μm), and a 50-nm-thick FIB section of a pure Ni crystal (Goodfellow) for calibration. Their edge energies were estimated by the zero of the second derivative of the smoothed XANES scans with 0.15- and 0.5-eV uncertainties for ID21 and ID16B, respectively.

SUPPLEMENTARY MATERIALS

Supplementary material for this article is available at http://advances.sciencemag.org/cgi/content/full/7/29/eabf3963/DC1

REFERENCES AND NOTES

1. S. A. Benner, E. A. Bell, E. Biondi, R. Brasser, T. Carell, H.-J. Kim, S. J. Mojzsis, A. Omran, M. A. Pasek, D. Trail, When did life likely emerge on Earth in an RNA-first process? *ChemSystemsChem* **2**, e1900035 (2020).
2. A. H. Knoll, Paleobiological perspectives on early microbial evolution. *Cold Spring Harb. Perspect. Biol.* **7**, a018093 (2015).
3. J. E. Javaux, Challenges in evidencing the earliest traces of life. *Nature* **572**, 451–460 (2019).
4. M. M. Walsh, D. R. Lowe, Filamentous microfossils from the 3500-My-old Onverwacht Group, Barberton Mountain Land, South Africa. *Nature* **314**, 530–532 (1985).
5. M. M. Tice, D. R. Lowe, Photosynthetic microbial mats in the 3416-Myr-old ocean. *Nature* **431**, 549–552 (2004).
6. D. Z. Oehler, M. M. Walsh, K. Sugitani, M. C. Liu, C. H. House, Large and robust lenticular microorganisms on the young Earth. *Precambrian Res.* **296**, 112–119 (2017).
7. K. Hickman-Lewis, F. Westall, B. Cavalazzi, Traces of early life from the Barberton Greenstone Belt, South Africa, in *Earth's Oldest Rocks* (Elsevier, ed. 2, 2019) pp. 1029–1058.
8. A. Hofmann, C. Harris, Silica alteration zones in the Barberton greenstone belt: A window into subseafloor processes 3.5–3.3 Ga ago. *Chem. Geol.* **257**, 221–239 (2008).
9. M. Ledevin, N. Arndt, A. Davaille, R. Ledevin, A. Simionovici, The rheological behaviour of fracture-filling cherts: Example of Barite Valley dikes, Barberton Greenstone Belt, South Africa. *Solid Earth* **6**, 253–269 (2015).
10. K. Abraham, A. Hofmann, S. F. Foley, D. Cardinal, C. Harris, M. G. Barth, L. André, Coupled silicon-oxygen isotope fractionation traces Archaean silicification. *Earth Planet. Sci. Lett.* **301**, 222–230 (2011).
11. W. Martin, J. Baross, D. Kelley, M. J. Russell, Hydrothermal vents and the origin of life. *Nat. Microbiol.* **6**, 805–814 (2008).
12. G. J. Dick, The microbiomes of deep-sea hydrothermal vents: Distributed globally, shaped locally. *Nat. Rev. Microbiol.* **17**, 271–283 (2019).
13. J. A. Baross, S. E. Hoffman, Submarine hydrothermal vents and associated gradient environments as sites for the origin and evolution of life. *Orig. Life Evol. Biosph.* **15**, 327–345 (1985).
14. M. J. Russell, N. T. Arndt, Geodynamic and metabolic cycles in the Hadean. *Biogeoscience* **2**, 97–111 (2005).
15. B. Damer, D. Deamer, Coupled phases and combinatorial selection in fluctuating hydrothermal pools: A scenario to guide experimental approaches to the origin of cellular life. *Life* **5**, 872–887 (2015).
16. T. C. Onstott, B. L. Ehlmann, H. Sapers, M. Coleman, M. Ivarsson, J. J. Marlow, A. Neubeck, P. Niles, Paleo-rock-hosted life on Earth and the search on Mars: A review and strategy for exploration. *Astrobiology* **19**, 1230–1262 (2019).
17. M. S. Dodd, D. Papineau, T. Grenne, J. F. Slack, M. Rittner, F. Pirajno, J. O'Neil, C. T. S. Little, Evidence for early life in Earth's oldest hydrothermal vent precipitates. *Nature* **543**, 60–64 (2017).
18. D. R. Lowe, G. R. Byerly, Stratigraphy of the west-central part of the Barberton Greenstone Belt, South Africa, in *Geologic Evolution of the Barberton Greenstone Belt, South Africa* (Geological Society of America, Special Paper 329, 1999), pp. 1–36.
19. M. T. Stiegler, D. R. Lowe, G. R. Byerly, Fragmentation and dispersal of komatiitic pyroclasts in the 3.5–3.2 Ga Onverwacht Group, Barberton greenstone belt, South Africa. *Geol. Soc. Am. Bull.* **123**, 1112–1126 (2011).
20. A. Hofmann, R. Bolhar, Carbonaceous cherts in the Barberton Greenstone Belt and their significance for the study of early life in the Archean record. *Astrobiology* **7**, 355–388 (2007).
21. J. W. Moreau, T. Sharp, A Transmission electron microscopy study of silica and kerogen biosignatures in ~1.9-Ga Gunflint microfossils. *Astrobiology* **4**, 196–210 (2004).
22. G. J. Colpas, M. J. Maroney, C. Bagyinka, M. Kumar, W. S. Willis, S. L. Suib, P. K. Mascharak, N. Baidya, X-ray spectroscopic studies of nickel complexes, with application to the structure of nickel sites in hydrogenases. *Inorg. Chem.* **30**, 920–928 (1991).
23. R. Buick, Microfossil recognition in Archean rocks: An appraisal of spheroids and filaments from a 3500-My-old chert-barite unit at North Pole, Western Australia. *Palaios* **5**, 441–459 (1990).
24. J. W. Schopf, A. B. Kudryavtsev, K. Sugitani, M. R. Walter, Precambrian microbe-like pseudofossils: A promising solution to the problem. *Precambrian Res.* **179**, 191–205 (2010).
25. K. Sugitani, K. Mimura, T. Nagaoka, K. Lepot, M. Takeuchi, Microfossil assemblage from the 3400 Ma Strelley Pool Formation in the Pilbara Craton, Western Australia: Results form a new locality. *Precambrian Res.* **226**, 59–74 (2013).
26. M. M. Walsh, Microfossils and possible microfossils from the Early Archean Onverwacht Group, Barberton Mountain Land, South Africa. *Precambrian Res.* **54**, 271–293 (1992).
27. A. H. Knoll, P. K. Strother, S. Rossi, Distribution and diagenesis of microfossils from the lower Proterozoic Duck Creek Dolomite, Western Australia. *Precambrian Res.* **38**, 257–279 (1988).
28. S.L. Cady, J.D. Farmer, *Evolution of Hydrothermal Ecosystems on Earth (And Mars?)* (Ciba Foundation Symposium 202, Wiley, 1996), pp.150–173.
29. F. Orange, F. Westall, J.-R. Disnar, D. Prieur, N. Bienvenu, M. Le Romancer, C. Défarge, Experimental silicification of the extremophilic Archaea *Pyrococcus abyssi* and *Methanocaldococcus jannaschii*: Applications in the search for evidence of life in early Earth and extraterrestrial rocks. *Geobiology* **7**, 403–418 (2009).
30. D. Z. Oehler, F. Robert, S. Mostefaoui, A. Meibom, M. Selo, D. S. McKay, Chemical mapping of Proterozoic organic matter at submicron spatial resolution. *Astrobiology* **6**, 838–850 (2006).
31. D. Wacey, S. Menon, L. Green, D. Gerstmann, C. Kong, N. Mcloughlin, M. Saunders, M. Brasier, Taphonomy of very ancient microfossils from the ~3400-Ma Strelley Pool formation and ~1900-Ma Gunflint formation: New insights using a focused ion beam. *Precambrian Res.* **220-221**, 234–250 (2012).
32. C. P. Marshall, E. A. Carter, S. Leuko, E. J. Javaux, Vibrational spectroscopy of extant and fossil microbes: Relevance for the astrobiological exploration of Mars. *Vib. Spectrosc.* **41**, 182–189 (2006).
33. M. A. van Zuilen, M. Chaussidon, C. Rollion-Bard, B. Marty, Carbonaceous cherts of the Barberton greenstone belt, South Africa: Isotopic, chemical, and structural characteristics of individual microstructures. *Geochim. Cosmochim. Acta* **71**, 655–669 (2007).
34. M. M. Walsh, D. R. Lowe, Modes of accumulation of carbonaceous matter in the early Archean: A petrographic and geochemical study of the carbonaceous cherts of the Swaziland Supergroup, in *Geologic Evolution of the Barberton Greenstone Belt, South Africa* (Geological Society of America, Special Paper 329, 1999), pp. 115–132.

35. L. Lemelle, P. Labrot, M. Salomé, A. Simionovici, M. Viso, F. Westall, In situ imaging of organic sulfur in 700–800-My-old. Neoproterozoic microfossils using x-ray spectromicroscopy at the S K-edge. *Org. Geochem.* **39**, 188–202 (2008).
36. M. E. L. Kohnen, J. S. Sinninghe Damsté, A. C. Kock-van Dalen, H. L. Ten Haven, J. Rullkötter, J. W. De Leeuw, Origin and diagenetic transformations of C_{25} and C_{30} highly branched isoprenoid sulphur compounds: Further evidence for the formation of organically bound sulphur during early diagenesis. *Geochim. Cosmochim. Acta* **54**, 3053–3063 (1990).
37. W. Nitschke, S. E. McGlynn, E. J. Milner-White, M. J. Russell, On the antiquity of metalloenzymes and their substrates in bioenergetics. *Biochim. Biophy. Acta* **1827**, 871–881 (2013).
38. K. Hickman-Lewis, B. Cavalazzi, S. Sorieul, P. Gautret, F. Foucher, M. J. Whitehouse, H. Jeon, T. Georgelin, C. S. Cockell, F. Westall, Metallomics in deep time and the influence of ocean chemistry on the metabolic landscapes of Earth's earliest ecosystems. *Sci. Rep.* **10**, 4965 (2020).
39. P. H. A. Timmers, C. U. Welte, J. J. Koehorst, C. M. Plugge, M. S. M. Jetten, A. J. M. Stams, Reverse methanogenesis and respiration in methanotrophic Archaea. *Archaea* , 1654237 (2017).
40. M. Krüger, A. Meyerdierks, F. O. Glöckner, R. Amann, F. Widdel, M. Kube, R. Reinhardt, J. Kahnt, R. Böcher, R. K. Thauer, S. Shima, A conspicuous nickel protein in microbial mats that oxidize methane anaerobically. *Nature* **426**, 878–881 (2003).
41. S. Scheller, M. Goenrich, R. Boecher, R. K. Thauer, B. Jaun, The key nickel enzyme of methanogenesis catalyses the anaerobic oxidation of methane. *Nature* **465**, 606–608 (2010).
42. A. L. Zerkle, C. H. House, S. L. Brantley, Biogeochemical signatures through times as inferred from whole microbial genomes. *Am. J. Sci.* **305**, 467–502 (2005).
43. P. Scherer, H. Lippert, G. Wolff, Composition of the major elements and trace elements of 10 methanogenic bacteria determined by inductively coupled plasma emission spectrometry. *Biol. Trace Elem. Res.* **5**, 149–163 (1983).
44. V. Cameron, C. H. House, S. L. Brantley, A first analysis of metallome biosignatures of hyperthermophilic archaea. *Archaea* **2012**, 789278 (2012).
45. J. B. Glass, S. Chen, K. S. Dawson, D. R. Horton, S. Vogt, E. D. Ingall, B. S. Twining, V. Orphan, Trace metal imaging of sulfate-reducing bacteria and methanogenic archaea at single-cell resolution by synchrotron x-ray fluorescence imaging. *Geomicrobiol. J.* **35**, 81–89 (2018).
46. E. K. Moore, B. I. Jelen, D. Giovannelli, H. Raanan, P. G. Falkowski, Metal availability and the expanding network of microbial metabolisms in the Archaean eon. *Nat. Geosci.* **10**, 629–636 (2017).
47. Q. Tang, P. E. Carrington, Y.-C. Horng, M. J. Maroney, S. W. Ragsdale, D. F. Bocian, X-ray absorption and resonance Raman studies of methyl-coenzyme M reductase indicating that ligand exchange and macrocycle reduction accompany reductive activation. *J. Am. Chem. Soc.* **124**, 13242–13256 (2002).
48. L. Lemelle, A. Simionovici, T. Schoonjans, R. Tucoulou, E. Enrico, M. Salomé, A. Hofmann, B. Cavalazzi, Analytical requirements for quantitative x-ray fluorescence nanoimaging of metal traces in solid samples. *Trends Anal. Chem.* **91**, 104–111 (2017).
49. J. M. García-Ruiz, E. Nakouzi, E. Kotopoulou, L. Tamborrino, O. Steinbock, Biomimetic mineral self-organization from silica-rich spring waters. *Sc. Adv.* **3**, e1602285 (2017).
50. C. Nims, J. Lafond, J. Alleon, A. S. Templeton, J. Cosmidis, Organic biomorphs may be better preserved than microorganisms in early Earth sediments. *Geology* **49**, 629–634 (2021).
51. Y. Ueno, K. Yamada, N. Yoshida, S. Maruyama, Y. Isozaki, Evidence from fluid inclusions for microbial methanogenesis in the early Archaean era. *Nature* **440**, 516–519 (2006).
52. F. Sun, W. Hu, X. Wang, J. Cao, B. Fu, H. Wu, S. Yang, Methanogen microfossils and methanogenesis in Permian lake deposits. *Geology* **49**, 13–18 (2021).
53. K. Nakamura, Y. Kato, A new geochemical approach for constraining a marine redox condition of Early Archean. *Earth Planet. Sci. Lett.* **261**, 296–302 (2007).
54. J. Krissansen-Totton, S. Olson, D. C. Catling, Disequilibrium biosignatures over Earth history and implications for detecting exoplanet life. *Sci. Adv.* **4**, eaao5747 (2018).
55. M. T. Hren, M. M. Tice, C. P. Chamberlain, Oxygen and hydrogen isotope evidence for a temperate climate 3.42 billion years ago. *Nature* **462**, 205–208 (2009).
56. K. J. Edwards, W. Bach, T. M. McCollom, Geomicrobiology in oceanography: Microbe-mineral interactions at and below the seafloor. *Trends Microbiol.* **13**, 449–456 (2005).
57. C. Petro, P. Starnawski, A. Schramm, K. U. Kjeldsen, Microbial community assembly in marine sediments. *Aquat. Microb. Ecol.* **79**, 177–195 (2017).
58. J. Fiebig, A. Stefánsson, A. Ricci, F. Tassi, F. Viveiros, C. Silva, T. M. Lopez, C. Schreiber, S. Hofmann, B. W. Mountain, Abiogenesis not required to explain the origin of volcanic hydrothermal hydrocarbons. *Geochem. Perspect. Lett.* **11**, 23–27 (2019).
59. M. C. Sforna, D. Brunelli, C. Pisapia, V. Pasini, D. Malferrari, B. Ménez, Abiotic formation of condensed carbonaceous matter in the hydrating oceanic crust. *Nat. Commun.* **9**, 5049 (2018).
60. W. S. Rasband, ImageJ, U.S. National Institutes of Health, Bethesda, MA, USA (1997–2018); https://imagej.nih.gov/ij/.
61. B. Cavalazzi, Chemotrophic filamentous microfossils from the Hollard Mound (Devonian, Morocco) as investigated by focused ion beam. *Astrobiology* **7**, 402–415 (2007).
62. D. Wacey, *Early Life on Earth: A Practical Guide* (Springer, 2009).
63. S. McMahon, Earth's earliest and deepest purported fossils may be iron-mineralized chemical gardens. *Proc. R. Soc. B* **286**, 20192410 (2019).
64. Y. Ueno, Y. Isozaki, H. Yurimoto, S. Maruyama, Carbon isotopic signatures of individual Archean microfossils(?) from Western Australia. *Int. Geol. Rev.* **43**, 196–212 (2001).
65. J. W. Schopf, K. Kitajima, M. J. Spicuzza, A. B. Kudryavtsev, J. W. Valley, SIMS analyses of the oldest known assemblage of microfossils document their taxon correlated carbon isotope compositions. *Proc. Natl. Acad. Sci. U.S.A.* **115**, 53–58 (2018).
66. M. Brasier, N. McLoughlin, O. Green, D. Wacey, A fresh look at the fossil evidence for early Archaean cellular life. *Philos. Trans. R. Soc. Lond. B Biol. Sci.* **361**, 887–902 (2006).
67. M. D. Brasier, O. R. Green, J. F. Lindsay, N. McLoughlin, A. Steele, C. Stoakes, Critical testing of Earth's oldest putative fossil assemblage from the ~3.5-Ga Apex Chert, Chinaman Creek Western Australia. *Precambrian Res.* **140**, 55–102 (2005).
68. F. U. Battistuzzi, A. Feijao, S. B. Hedges, A genomic timescale of prokaryote evolution: Insights into the origin of methanogenesis, phototrophy, and the colonization of land. *BMC Evol. Biol.* **4**, 44 (2004).
69. K.-U. Hinrichs, Microbial fixation of methane carbon at 2.7 Ga: Was an anaerobic mechanism possible? *Geochem. Geophys. Geosyt.* **3**, 1–10 (2002).
70. D. R. Lowe, G. R. Byerly, The nonglacial and noncratonic origin of an early Archean felsic volcaniclastic unit, Barberton Greenstone Belt, South Africa. *Precambrian Res.* **341**, 105647 (2020).
71. A. Kröner, J. E. Hoffmann, H. Xie, F. Wu, C. Muenker, E. Hegner, J. Wong, Y. Wan, D. Liu, Generation of early Archaean felsic greenstone volcanic rocks through crustal melting in the Kaapvaal craton, southern Africa. *Earth Planet. Sci. Lett.* **381**, 188–197 (2013).
72. G. R. Byerly, A. Kröner, D. L. Lowe, W. Todt, M. M. Walsh, Prolonged magmatism and time constraints for sediment deposition in the early Archean Barberton greenstone belt: Evidence from the Upper Onverwacht and Fig Tree groups. *Precambrian Res.* **78**, 125–138 (1996).
73. A. Kröner, G. R. Byerly, D. R. Lowe, Chronology of early Archaean granite-greenstone evolution in the Barberton Mountain Land, South Africa, based on precise dating by single zircon evaporation. *Earth Planet. Sci. Lett.* **103**, 41–54 (1991).
74. M. J. Viljoen, R. P. Viljoen, Evidence for the existence of a mobile extrusive peridotitic magma from the Komati Formation of the Onverwacht Group. *Special Publication Geol. Soc. South Africa* **2**, 87–112 (1969).
75. J. Veizer, J. Hoefs, D. R. Lowe, P. C. Thurston, Geochemistry of Precambrian carbonates: II. Archean greenstone belts and Archean sea water. *Geochim. Cosmochim. Acta* **53**, 859–871 (1989).
76. A. Hofmann, R. Bolhar, B. Orberger, F. Foucher, Cherts of the Barberton greenstone belt, South Africa: Petrology and trace-element geochemistry of 3.5- to 3.3-Ga-old silicified volcaniclastic sediments. *South Afr. J. Geol.* **116**, 297–322 (2013).
77. C. Rollion-Bard, N. Vigier, S. Spezzaferri, In situ measurements of calcium isotopes by ion microprobe in carbonates and application to foraminifera. *Chem. Geol.* **244**, 679–690 (2007).
78. J. W. Schopf, A. B. Kudryavtsev, Biogenicity of Earth's earliest fossils: A resolution of the controversy. *Gondw. Res.* **22**, 761–771 (2012).
79. A. Knoll, Recognition of a biological signatures in rock. Discussion summary, in *Size Limits of Very Small Microorganisms: Proceedings of a Workshop* (National Academy Press, 1999), pp. 85–87.
80. J. Rouillard, M. van Zuilen, C. Pisapia, J.-M. Garcia-Ruiz, An alternative approach for assessing biogenicity. *Astrobiology* **21**, 151–164 (2021).
81. B. Wopenka, J. D. Pasteris, Structural characterization of kerogens to granulite-facies graphite: Applicability of Raman microprobe spectroscopy. *Am. Mineral.* **78**, 533–557 (1993).
82. O. Beyssac, B. Goffé, C. Chopin, J. N. Rouzaud, Raman spectra of carbonaceous material in metasediments: A new geothermometer. *J. Metam. Geol.* **20**, 859–871 (2002).
83. D. G. Henry, I. J. Jarvis, G. Gillmore, M. Stephenson, Raman spectroscopy as a tool to determine the thermal maturity of organic matter: Application to sedimentary, metamorphic and structural geology. *Earth Sci. Rev.* **198**, 102936 (2019).
84. J. M. Rahl, K. M. Anderson, M. T. Brandon, C. Fassoulas, Raman spectroscopic carbonaceous material thermometry of low-grade metamorphic rocks: Calibration and application to tectonic exhumation in Crete, Greece. *Earth Planet. Sci. Lett.* **240**, 339–354 (2005).

85. M. Aoya, Y. Kouketsu, S. Endo, H. Shimizu, T. Mizukami, D. Nakamura, S. Wallis, Extending the applicability of the Raman carbonaceous material geothermometer using data from contact metamorphic rocks. *J. Metam. Geol.* **28**, 895–914 (2010).
86. Y. Kouketsu, T. Mizukami, H. Mori, M. Endo, M. Aoya, H. Hara, D. Nakamura, S. Wallis, A new approach to develop the Raman carbonaceous material geothermometer for low-grade metamorphism using peak width. *Island Arc* **23**, 33–50 (2014).
87. M. Cotte, E. Pouyet, M. Salomé, C. Rivard, W. De Nolf, H. Castillo-Michel, T. Fabris, L. Monico, K. Janssens, T. Wang, P. Sciau, L. Verger, L. Cormier, O. Dargaud, E. Brun, D. Bugnazet, B. Fayard, B. Hesse, A. E. P. del Real, G. Veronesi, J. Langlois, N. Balcar, Y. Vandenberghe, V. A. Solé, J. Kieffer, R. Barrett, C. Cohen, C. Cornu, R. Baker, E. Gagliardini, E. Papillona, J. Susini, The ID21 x-ray and infrared microscopy beamline at the ESRF: Status and recent applications to artistic materials. *J. Anal. At. Spectrom.* **32**, 477–493 (2017).
88. G. Martínez-Criado, J. Villanova, R. Tucoulou, D. Salomon, J.-P. Suuronen, S. Labouré, C. Guilloud, V. Valls, R. Barrett, E. Gagliardini, Y. Dabin, R. Baker, S. Bohic, C. Cohen, J. Morse, ID16B: A hard x-ray nanoprobe beamline at the ESRF for nanoanalysis. *J. Synchrotron Radiat.* **23**, 344–352 (2016).
89. A. Simionovici, C. Schroer, L. Lemelle, *International Tables for Crystallography: Volume I, X-ray Absorption Spectroscopy and Related Techniques of IUCr Series C* (Wiley & Blackwell, 2021), pp. 1–10.
90. A. N. Mansour, C. A. Melendes, Analysis of x-ray absorption spectra of some nickel oxycompounds using theoretical standards. *J. Phys. Chem. A* **102**, 65–81 (1998).
91. R. T. Wilkin, D. A. Rogers, Nickel sulfide formation at low temperature: Initial precipitates, solubility, and transformation products. *Environ. Chem.* **7**, 514–523 (2010).
92. G. Jahrsengene, H. C. Wells, C. Sommerseth, A. P. Ratvik, L. P. Lossius, K. H. Sizeland, P. Kappen, A. M. Svensson, R. G. Haverkamp, An EXAFS and XANES Study of V, Ni, and Fe speciation in cokes for anodes used in aluminum production. *Metall. Mater. Trans. B* **50**, 2969–2981 (2019).
93. V. A. Solé, E. Papillon, M. Cotte, P. Walter, J. Susini, A multiplatform code for the analysis of energy-dispersive x-ray fluorescence spectra. *Spectrochim. Acta B* **62**, 63–68 (2007).

Acknowledgments: We thank L. Boarino, R.J. Colby, C. Chaduteau, and G. Landais for technical assistance. We are also grateful to J. Eksteen and P. Mokoena and the Mpumalanga Parks Board, for access and permission to sample. **Funding:** The research was supported by the FP7-PEOPLE-CIG grant no. 618657 to B.C., by NASA NAI-CAN7 16BB06I to S.L.C., and by the French National Research Agency ANR-15-IDEX-02 to A.S. and L.L. We are grateful to the CNES and ESRF facility (proposals ES108, ES231, and ES346). A portion of the research was performed using the EMSL (grid.436923.9), a DOE Office of Science User Facility sponsored by the Biological and Environmental Research program. This research received support from the Europlanet 2024 RI, which has received funding from the European Union's Horizon 2020 research innovation programme grant no. 871149. **Author contributions:** B.C. and A.H. conceptualized the work. A.H. performed the field campaign and collected samples. B.C., A.H., and S.L.C. performed the optical microscope observations. E.T., A.H., and N.B. performed LG-SIMS using IRMS data acquisition and interpretation. B.C. and R.C. performed ToF-SIMS interpretations. B.C., E.B., and A.Mar. performed Raman data acquisition and interpretation. B.C. and E.E. prepared the FIB sections; B.C. and S.L.C. performed TEM interpretations; L.L., A.S., A.Man., M.S., R.T., B.C., and E.E. performed synchrotron data acquisition and interpretation. All authors contributed to and approved the submitted manuscript. **Competing interests:** The authors declare that they have no competing interests. **Data and materials availability:** All data needed to evaluate the conclusions in the paper are present in the paper and/or the Supplementary Materials. Additional data related to this paper may be requested from the authors.

Submitted 23 October 2020
Accepted 28 May 2021
Published 14 July 2021
10.1126/sciadv.abf3963

Citation: B. Cavalazzi, L. Lemelle, A. Simionovici, S. L. Cady, M. J. Russell, E. Bailo, R. Canteri, E. Enrico, A. Manceau, A. Maris, M. Salomé, E. Thomassot, N. Bouden, R. Tucoulou, A. Hofmann, Cellular remains in a ~3.42-billion-year-old subseafloor hydrothermal environment. *Sci. Adv.* **7**, eabf3963 (2021).